ACS Catalysis

pubs.acs.org/acscatalysis

Research Article

Synthesis–Structure–Activity Relationship in Cu-MOR for Partial Methane Oxidation: Al Siting via Inorganic Structure-Directing Agents

Sebastian Prodinger,* Karoline Kvande, Bjørnar Arstad, Elisa Borfecchia, Pablo Beato, and Stian Svelle

Cite This: ACS Catal. 2022, 12, 2166–2177

Read Online

ACCESS | Metrics & More | Article Recommendations | Supporting Information

ABSTRACT: In the pursuit of controlling the propensity of Cu-mordenite (MOR) for the selective oxidation of CH_4, we take a closer look at intrinsic zeolite parameters. Via synthesis design, we vary the relative proportion of Al situated near the 8-rings and 12-rings of MOR zeolite. This is accomplished using different Al sources impacting the local degree of silica dissolution and zeolite formation as evidenced by crystallization times and morphological differences. Interrogating the crystalline system with steric probe molecules in conjunction with spectroscopic techniques such as ^{1}H magic angle spinning (MAS) NMR, infrared spectroscopy, as well as temperature-programmed desorption confirms discrete changes of the Al within the unit cell. The subsequent copper exchange allows for the generation of Cu-MOR materials of different inclinations for the activation of methane in the stepwise formation of MeOH. Here, an increasing degree of acid sites in more easily accessible locations (e.g., 12-ring) correlates with increasing maximum productivity toward MeOH at moderate exchange degrees. X-ray absorption spectroscopy supports this notion, finding a higher concentration of self-reduction-resistant framework-associated Cu^{2+} species, previously established as the active sites in the selective oxidation of CH_4.

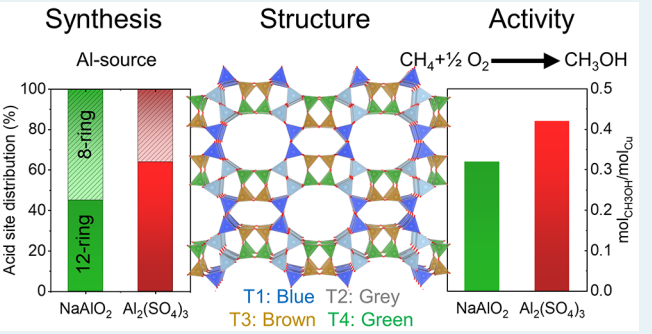

KEYWORDS: *methane–methanol, copper zeolite, synthesis, Al siting, mordenite, pH*

1. INTRODUCTION

Small alkanes, such as CH_4, are potent greenhouse gases contributing to climate change. Released primarily by the large-scale venting of natural gas,[1] waste-CH_4 (and other small alkanes) mitigation is also necessary to address their generation during the upcycling of plastics,[2] biogas leaking from municipal waste (35–75% CH_4),[3] and the potential release of CH_4 from clathrates on ocean floors and entrapped in thawing permafrost. The challenge lies in the strong C–H bond with a bond dissociation energy (BDE) of 435 kJ/mol posing a large energy barrier for H-abstraction.[4] This traditionally requires complete disassembly of the CH_4 molecule in large-scale, energy-intensive steam reforming facilities. Yet, the remote and distributed location of the gaseous waste-CH_4 feedstock precludes the use of this centralized chemical industry. To address all of these challenges, groundbreaking selective oxidation technology—deployed in modular unit operations—is crucial.

Mastery of the selective oxidation of CH_4 requires the isolation of the reactive MeOH intermediate, ideally using inexpensive oxygen. Groothaert et al. were the first to report a heterogeneous system—a zeolite—containing a copper moiety able to activate oxygen at low temperatures and selectively oxidize CH_4.[5] Among the various types of zeolite frameworks investigated, the mordenite system (MOR) appears to achieve exceptionally high MeOH yields. When accounting for how many moles of MeOH are produced under atmospheric conditions per moles of copper used (i.e., MeOH productivity), the MOR system tends to outperform other systems such as MFI, CHA, and FER.[6,7] Note that this empirical trend holds true for the stoichiometric, stepwise process, while the site-specific rates of the continuous, catalytic process appear to favor small-pore CHA over the MOR system.[8,9]

An interesting feature in the MOR system is the 8-ring channel that runs in parallel to the 12-ring pore.[10] The distorted nature of the 8-ring (5.7 × 2.6 Å) prevents molecules from entering it alongside the 12-ring. However, it is possible to access this cavity via an 8-ring (3.4 × 4.8 Å) situated perpendicular to the 12-ring within the zeolite framework. As a result, MOR can be considered a one-dimensional zeolite with

Received: November 5, 2021
Revised: January 12, 2022
Published: January 28, 2022

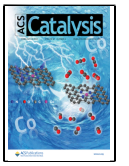

a large-pore 12-ring and an internal, small-pore 8-ring side pocket. The latter has been identified by Grundner et al. to impart effectiveness to the resulting Cu species.[11] They conclude that the active copper is present as a Cu-oxo trimeric species (with a productivity of 0.3 mol_{MeOH}/mol_{Cu}). Other groups later observed productivities of 0.5, which they associated with dimeric Cu-oxo species,[12−14] also inferred from spectroscopic means. This highlights the uncertainty still concerning the Cu-MOR system and its active site motif for CH_4 to MeOH oxidation.

Recently, it has been suggested that the location of the Cu-oxo system within the MOR zeolite can also influence the reaction outcome. Solomon et al. modeled the tendency of a $[Cu_2O]^{2+}$ species to activate CH_4 by abstracting a hydrogen atom, finding that a more constricted space in the 8-ring is favorable.[15] Lercher et al. then demonstrated the possibility for activating an additional oxygen in their proposed Cu_3O_3 motif by increasing the chemical potential (i.e., CH_4 pressure), and also modeled the location of this Cu-oxo species to influence the Gibbs free energy for CH_4 activation.[16] Davis et al. showed that when using Na-exchanged MOR instead of H^+-exchanged MOR, the Cu species occupy different sites, leading to a lower overall selectivity toward MeOH.[17] They hypothesized that the Na^+ cations populate the 8-ring exchange sites, pushing the Cu-oxo sites closer to the 12-ring. The larger space available promotes the formation of less selective Cu-peroxo species. Previously, Dyballa et al. also noted a lower productivity for a Cu,Na-MOR system over a Cu,H-MOR system; however, the MeOH selectivity was equally high.[12,18] These results suggest that not all MOR zeolite supports are comparable and that control over the location of Cu-oxo species, via synthesis design, could enable the tuning of the oxidation potential of the resulting Cu zeolites.

A distinctive feature for MOR is its four crystallographically unique T-sites, of which one (T3) has been identified as preferred for Al incorporation.[19] Most noteworthy, this T-site is situated deep within the 8-ring side pocket. Varying the location of Al within a zeolite framework is an ambitious endeavor due to the metastable nature of zeolites and the need to kinetically isolate the most favorable composition. Recent efforts have focused on influencing Al distributions in high-silica zeolites such as SSZ-13 and ZSM-5.[20−24] This has been primarily achieved using a combination of low-charge-density organic structure-directing agents (OSDA) and high-charge-density inorganic cations.[25] The use of alcohols has also been shown to alter the incorporation location of Al.[26] For the stepwise oxidation of CH_4 to MeOH, Al-rich systems (Si/Al < 10) are desirable, generating, in their Cu form, high CH_3OH yields. However, their synthesis typically precludes the use of ionic OSDA posing a challenge to Al siting attempts. In the case of Al-rich MOR, it should be noted that the scientific literature historically used to differentiate between a small-port and large-port MOR variant, implying low (<0.1 cm^3/g) and high microporosities (>0.1 cm^3/g), respectively.[27] Note that Knorpp et al. have recently revisited this distinction finding large-port Cu-MOR to be more efficient at selectively oxidizing CH_4.[28] Results by Lu et al. indicate that this port size distinction can be influenced by the Al source, and upon exchange of Na^+ with the smaller Li^+, small-port Na-MOR can be converted into large-port Li-MOR.[29] Building on these observations, we posit that the Al source in highly alkaline syntheses can be used to influence the Al distribution within MOR zeolites. Subsequently, we will show how this impacts the propensity of the resulting Cu-oxo species for the selective oxidation of CH_4.

2. RESULTS AND DISCUSSION

2.1. Characterization of As-Made Zeolites. We investigated the synthesis of MOR using four different Al sources, $NaAlO_2$, $Al(OH)_3$, $Al(NO_3)_3$, and $Al_2(SO_4)_3$. In all cases, gel composition and crystallization temperature (170 °C) were held constant varying only the Al source. The crystallization was followed by periodically removing autoclaves from the oven and studying the degree of crystallinity, and ultimately pure MOR phase was isolated in all cases, as assessed by X-ray diffraction (Figure S1). The resulting materials were all found to be highly crystalline MOR; however, physicochemical differences can be observed depending on the Al source (Table 1).

Table 1. Impact of Varying the Al Source on the pH of the Synthesis Gel, Crystallization Time, Solid Yield, and Si/Al of the Resulting MOR Pure Crystal Phase[a]

Al source	pH_{gel}	crystallization time (h)	solid yield (%)	Si/Al
$Al(OH)_3$	>14.5	24	51	6.7
$NaAlO_2$	14.35	48	59	6.3
$Al(NO_3)_3$	14.20	67	84	9.2
$Al_2(SO_4)_3$	14.10	88	88	9.1

[a]The gel composition was 5.9 Na_2O:Al_2O_3:28 SiO_2:318 H_2O.

Most significantly, the pH of the synthesis prior to crystallization varied slightly. The pH is typically a function of the mineralizer agents (i.e., NaOH) concentration. A high pH (i.e., a high NaOH concentration) facilitates rapid depolymerization of the amorphous SiO_2 source needed to enable the formation of small aluminosilicate building units that subsequently reorganize and crystallize into larger zeolitic segments.[30,31] It follows that the lower pH observed for $Al(NO_3)_3$ and $Al_2(SO_4)_3$ results in the observed longer crystallization time that also includes a prolonged induction period during which no X-ray visible crystals are observed. In addition to the crystallization time, another aspect that is seemingly affected by the choice of the Al source is the yield of the crystalline phase. Higher yields are measured for the gels of lower alkalinity. Tracing the crystallization process by recording the solid yield infers that the amorphous precursor is highly stable under alkaline conditions (Figure S1). de Jong et al. have noted that MOR synthesis proceeds via a reorganization/dissolution of an aluminosilicate gel rather than a silica gel.[32] Once a sufficient degree of crystalline material is formed, the solid yield drops. We hypothesize that the higher pH for $Al(OH)_3$ and $NaAlO_2$ is seemingly enough to dissolve part of the crystalline material, resulting in a lower yield of the zeolite phase. This dissolution also results in a lower Si/Al compared to both the initial gel ratio (Si/Al_{gel} 14) and compared to the gels of lower alkalinity ($Al(NO_3)_3$ and $Al_2(SO_4)_3$), implying less Si retention. It should be noted that the molarity of the mineralizer agent, NaOH, was held constant in all syntheses, implying that it is the Al source that affects the pH. The structure of Al in aqueous conditions can vary depending on the pH; however, under such highly alkaline conditions, it is always present as $Al(OH)_4^-$.[33,34] Thus, we can specify that the pH-induced differences in the materials must be associated with the role of the inorganic Al salt's anion. The Al salts dissociate, releasing, in the case of $Al(NO_3)_3$ and $Al_2(SO_4)_3$,

https://doi.org/10.1021/acscatal.1c05091
ACS Catal. 2022, 12, 2166−2177

the weak conjugate bases of strong acids. Unlike strong conjugate bases (e.g., OH^-), they do not increase the pH. While the pH meter only detects the pH in the bulk of the gel, we speculate these differences to be more pronounced in the local environment of the amorphous precursor's pores. Here, the degree of supersaturation and thus the rate of crystallization as well as the mode of crystal growth will vary. Differences in crystal growth are evident from inspecting the crystals with scanning electron microscopy (SEM, Figure 1).

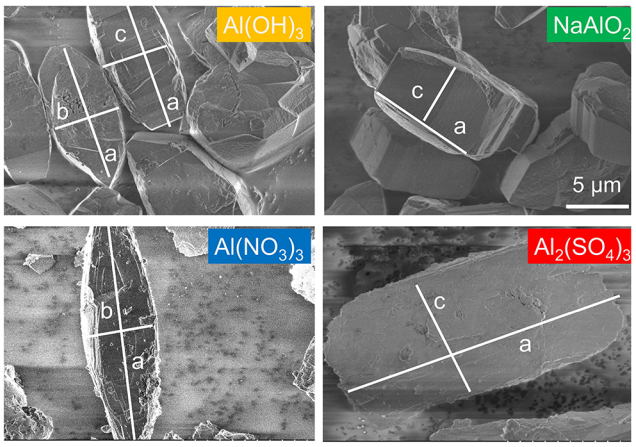

Figure 1. Representative scanning electron micrographs of the as-synthesized MOR zeolites. Crystal axes are annotated. The prismatic crystals show different aspect ratios (Figure S2) depending on the Al sources used.

In all four syntheses, micron-sized MOR crystals (>10 μm) were obtained that have well-defined facets forming prismatic bulk crystals without significant intergrowth. The large crystal size is due to the low water content during the hydrothermal synthesis.[32] At the same time, the slower crystallization kinetics of the less basic Al salts also results in larger particle sizes (20 vs 12 μm for the longest axis, the *a*-axis). Measuring the aspect ratios (L_c/L_b and L_c/L_a) suggests a slight inclination toward preferential crystal growths along the *a* and *c*-axes at the expense of the *b*-axis for syntheses at a lower alkalinity (Figure S2). For MOR, the *c*-axis is assigned to the direction of the 12-ring channel, implying that the *b*-axis would follow the orthogonal 8-ring side pocket. Recently, Valtchev et al. have shown how adding NH_4F in ZSM-5 synthesis significantly reduces growth along the *b*-axis, allowing for easier diffusion along the straight channels in the zeolite.[35] Growth modification can also be achieved by surfactants,[36] as well as reactivity differences of the Si source.[37]

Subtle changes are also observed for the specific surfaces areas assessed with N_2 adsorption at −196 °C (Table S2), with the more alkaline systems ($NaAlO_2$, $Al(OH)_3$) having slightly lower surface areas (400 vs 450 m^2/g). However, as their micropore volumes are above 0.1 cm^3/g, all MOR systems are classified as large-port MOR. Upon transformation of Na-MOR into the H-MOR system, the surface areas and pore volumes increase to ca. 500 m^2/g for all samples irrespective of the Al source. This increase is suggestive of pore blockage due to the larger Na^+ cations in the one-dimensional system. At the same time, it also points toward an enrichment of Na^+ (and thus framework Al) in certain areas, leading to a lower porosity for the more alkaline systems.

2.2. Determination of the Acid Site Distribution. To obtain an active Cu-MOR system necessitates the ion exchange with aqueous Cu^{2+} salts that titrate and exchange the H^+ balancing the negative framework charge induced by isomorphously substituted Al. Hence, the location of the Cu exchange sites, the Brønsted acid sites, and the underlying Al distribution are intrinsically linked, and determining any of these will yield insight into the remaining unknowns. Interrogating Al distributions is complicated by multiple T-sites (such as in ZSM-5) as recently summarized by Bickel et al.[38] It requires UV−vis spectroscopy in conjunction with Co^{2+} ions and coupled with temperature-programmed desorption (TPD) techniques to determine the amount of paired Al in SSZ-13 and ZSM-5 zeolites.[20,22] In the past, Vjunov et al. have also successfully used a combination of Al MAS NMR, Al-extended X-ray absorption fine structure (EXAFS), and density functional theory (DFT) modeling to determine the Al distribution in BEA zeolite.[39]

2.2.1. Temperature-Programmed Desorption (TPD). In the case of MOR, we are exploiting the markedly different pore systems of the 12-ring and 8-ring to elucidate differences among the synthesized zeolite systems. Temperature-programmed desorption (TPD) utilizing a small probe molecule such as NH_3 (kinetic diameter 2.6 Å) can be a powerful technique to quantify acid sites in the synthesized zeolites. Starting with the NH_4 form of the zeolites, we initially

Table 2. Elemental Composition of Synthesized MOR[a]

H-MOR (Si/Al & Al source)	Al concentration (μmol/g)[b]	extra-framework Al (Al^{VI}) (μmol/g)[b]	framework Al (Al^{IV}) (μmol/g)[b]	acid site concentration$_{TPD}$ (μmol/g)[b]			accessibility index (%)[c]
				NH_4^+	NH_3	*n*-propylamine	
MOR7-$Al(OH)_3$	2165	450	1715	2090	1460	730	43 ± 3
MOR6-$NaAlO_2$	2260	430	1830	2090	1530	830	45 ± 3
MOR9-$Al(NO_3)_3$	1640	290	1350	1590	1390	840	63 ± 4
MOR9-$Al_2(SO_4)_3$	1660	340	1320	1460	1360	840	64 ± 4
MOR6 commercial	2150	430	1720	2070	1440	1190	69 ± 4
MOR8-$NaAlO_2$	1890	360	1530	1700	1400	660	44 ± 3
MOR8-$Al_2(SO_4)_3$	1850	350	1500	1620	1320	820	56 ± 3

[a]Total Al concentration (from elemental analysis) and tetrahedral Al (Al^{IV}, from ^{27}Al MAS NMR) are in good agreement with the concentration determined via temperature-programmed desorption of the NH_4 form and titration of Brønsted acid sites with NH_3. A more sterically hindered probe, *n*-propylamine, titrates only a fraction of the sites postulated to be more accessible sites in the 12-ring opposed to the 8-ring. We define the accessibility index (AI)-acid sites from *n*-propylamine with respect to the tetrahedral Al concentration. The accessibility index varies across the investigated MOR samples. [b]Uncertainty: ±5%. [c]$BAS_{n\text{-propylamine}}/Al^{(IV)}$.

https://doi.org/10.1021/acscatal.1c05091
ACS Catal. 2022, 12, 2166−2177

quantified the NH_3 released during the decomposition of the NH_4^+-charge-balancing cation. This allows us to determine the total amount of Al (i.e., theoretical maximum H^+ concentration) in the framework, with the concentration being in excellent agreement with the Al concentration obtained via elemental analysis from microwave plasma atomic emission spectroscopy (MP-AES) (Table 2). The small discrepancy (ca. 10%) is attributed to adsorbed water on the zeolite, in agreement with thermogravimetric analysis (TGA, not shown).

The decomposition of NH_4^+ at high temperatures leads to the formation of extra-framework Al as evidenced from ^{27}Al MAS NMR (Figure S8). Integration of the spectra for all samples in their hydrated state allowed us to quantify the amount of extra-framework Al in the form of octahedral hexaaqua Al species at 0 ppm being comparable for all protonic zeolites (Table 2). Extra-framework Al can exist in many different states;[40] however, it no longer behaves as a Brønsted acid or ion exchange site. Therefore, following the NH_4^+-decomposition TPD, we performed an NH_3 adsorption step during which NH_3 chemisorbs on the in situ generated Brønsted acid sites. Prior to the TPD step, the sample is flushed with a stream of inert N_2 at 170 °C, which removes weakly bound physisorbed NH_3 and NH_3 from Lewis acid sites.[41] This ensures that the Lewis acidic extra-framework Al does not conflate the total number of Brønsted acid sites probed. The titrated amount of NH_3 on Brønsted acid sites can be compared to the concentration of tetrahedral Al obtained by subtracting the amount of extra-framework Al (from ^{27}Al MAS NMR) from the total Al concentration measured with MP-AES. Once more, we achieve a very good agreement across the quantification techniques.

As the Si/Al ratio decreases, the TPD profile (Figure S4) shows an increasing contribution of NH_3 desorbed at lower temperatures (300 vs 475 °C), suggestive of the weaker acid strength associated with an increasing number of Al as next nearest neighbor.[42] As a result, it is conceivable for the inert flushing period to remove more NH_3 adsorbed on weaker sites, leading to a higher discrepancy between titrated acid sites titrated and those theoretically available based on ^{27}Al MAS NMR and MP-AES. Sodium back-exchange into the NH_4 form does after all suggest that 95% of all Al is exchangeable, irrespective of the Al source (Figure S13b).

n-Propylamine is another base molecule that can be used to titrate acid sites. It is only sensitive to Brønsted acid sites that upon heating catalyze a Hoffman-type elimination reaction releasing propene, directly correlated with the Brønsted acid site concentration.[43] The propylamine molecule is larger than NH_3, allowing for discrimination in acid site locations. It has been observed that propylamine is able to titrate all sites in 10-ring ZSM-5, however, only a fraction thereof in the small-pore SSZ-13, as the molecule is hindered by diffusion through the 8-ring window.[41] We observe a similar differentiation in MOR, with propylamine TPD leading to lower concentrations of acid sites compared to NH_3 TPD (Table 2). Based on the similarities with the small-pore SSZ-13 zeolite, we suggest that propylamine cannot access acid sites in the 8-ring with the caveat that we cannot exclude the possibility of acid site titration in the 8-ring pore mouth. Yet, the origin of the zeolite sample affects the amount of Brønsted sites available for titration by propylamine. We find that MOR crystallized from using $NaAlO_2$ and $Al(OH)_3$ in the synthesis gel contains a higher contribution of acid sites in the 8-ring, compared to using $Al(NO_3)_3$ and $Al_2(SO_4)_3$. We define the ratio between acid sites quantified with propylamine and tetrahedral Al from ^{27}Al MAS NMR, the accessibility index (AI, Table 2). This descriptor neatly suggests that in accordance with the morphological differences described in the previous section, the choice of Al source and pH affects the intrinsic zeolite properties. Interestingly, the acid site properties of a commercial sample (CBV10Ads), previously used to generate the highly active Cu-MOR material,[13] are in agreement with the latter two Al sources.

2.2.2. Diffuse Reflectance Infrared Fourier Transform Spectroscopy (DRIFTS). To corroborate the evidence for differing Al distributions in MOR, we performed additional characterization of the materials, mainly with infrared (IR) and solid-state NMR spectroscopy. Previously, IR spectroscopy has been utilized to highlight spatial differences in the acid sites of MOR by probing the stretching vibrations of the bridging hydroxyls.[44,45] The band located at 3605 cm^{-1} can be deconvoluted into two species at 3610 and 3590 cm^{-1} associated with acid sites in the 12-ring and 8-ring, respectively (Figure 2).[44,45] As the large crystal size of the synthesized

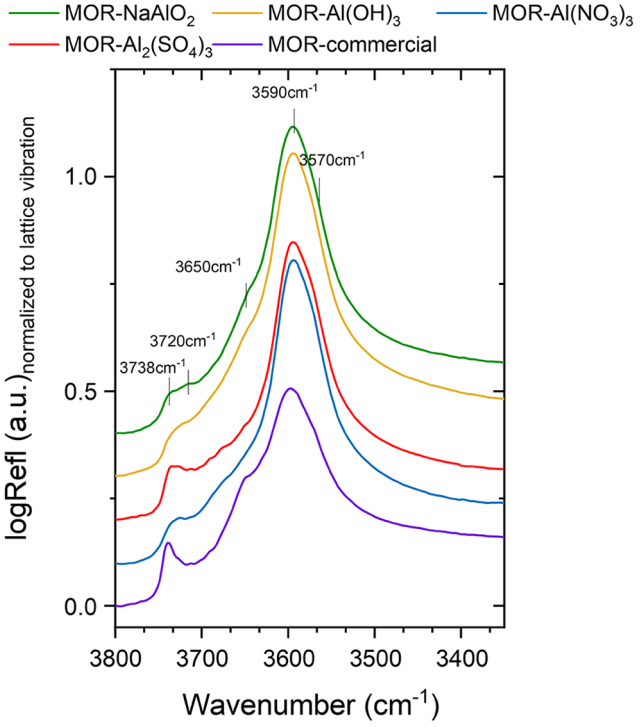

Figure 2. DRIFTS spectra of the hydroxyl region for the protonic forms of MOR synthesized in-house and commercially available (CBV10Ads). The spectra are normalized to the lattice vibrations (2090−1750 cm^{-1}, not shown) and shifted vertically. Spectra are collected at 380 °C under atmospheric conditions.

MOR prevented the use of transmission mode, the measurements were performed in diffuse reflectance mode (DRIFTS). The range of hydroxyl bands observed can be assigned to bridging hydroxyls (3600 cm^{-1}), hydroxyls associated with extra-framework Al (3650 cm^{-1}), and those belonging to internal and external silanol groups (3720 and 3740 cm^{-1}, respectively).[46] The smaller crystal size of the commercial H-MOR (CBV10Ads) is evident from the higher contribution of external SiOH, relative to the bridging hydroxyls. MOR9-$Al_2(SO_4)_3$ and MOR9-$Al(NO_3)_3$ also exhibit a slightly higher

https://doi.org/10.1021/acscatal.1c05091
ACS Catal. 2022, 12, 2166−2177

contribution of external SiOH compared to MOR synthesized under more alkaline conditions, which we tentatively attribute to the larger external surface area generated by the preferential crystal growth along the *a*-axis.

In agreement with vibrations of two distinct bridging hydroxyl groups, the asymmetric nature of the 3600 cm^{-1} peak is self-evident. Note that the spectra are collected at high temperatures, leading to a redshift compared to those typically reported at room temperature. Deconvolution of the spectra into three main components assigned to bridging hydroxyls in the 8-ring (3570 cm^{-1}), 12-ring (3590 cm^{-1}), and Al-OH (3650 cm^{-1}) supports the data obtained from TPD results (Figure S5). MOR synthesized with $NaAlO_2$ or $Al(OH)_3$ has a higher preference for incorporating acid sites in the 8-ring, compared to $Al(NO_3)_3$ and $Al_2(SO_4)_3$. Most noteworthily, commercial H-MOR follows the latter two Al sources, repeating the trend first substantiated with TPD.

2.2.3. Magic Angle Spinning NMR (MAS NMR). Unlike DRIFTS, ^{1}H MAS NMR is a powerful technique not susceptible to erroneous surface effects. A quantitative assessment of protons can be achieved by evaluating spectra of the dehydrated MOR (Figure S6). Similar to the DRIFTS spectra, the most pronounced feature belongs to the bridging hydroxyls (3.8 ppm).[47,48] Additional peaks up- and downfield are assigned to SiOH (1.9 ppm), AlOH (2.6 ppm), and more distorted protons (6−9 ppm), respectively. These distorted protons are likely coordinated to residual, strongly bound water molecules.[49−51] As observed with DRIFTS, the main difference between MOR9-$Al_2(SO_4)_3$ and MOR6-$NaAlO_2$ is the higher relative concentration of Al-OH and SiOH groups in the latter. Quantification of octahedral, extra-framework Al with ^{27}Al MAS NMR (Figure S8) resulted in largely the same amount for all synthesized MOR. Note that the discrepancy to the ^{1}H MAS NMR and DRIFTS data can be rationalized by the presence of small extra-framework Al clusters.[40,52] Furthermore, it is possible for some more distorted Al to be broadened beyond detection at this field strength.[53,54]

^{1}H MAS NMR by itself is not able to resolve spatial differences between the bridging hydroxyl groups (3.8 ppm). To achieve spatial resolution, Zheng et al. suggest the use of the weak base molecule, deuterated acetonitrile (CD_3CN).[49] The small size of this probe molecule (3.9 Å kinetic diameter) should allow it to diffuse into the small 8-ring pore channel via the side pocket (3.4 × 4.8 Å) and titrate those acid sites in addition to those present in less confined places of the 12-ring. To ensure complete titration of acid sites, the dehydrated sample was exposed to CD_3CN vapors at room temperature until equilibration was achieved, followed by a rapid degassing of physisorbed CD_3CN. The resulting ^{1}H MAS NMR spectra exhibit the presence of two new peaks at ca. 10.5 and 12.5 ppm at the expense of the peak at 3.8 ppm while leaving the remaining peaks untouched (Figure 3).

Zheng et al. assigned the two peaks at 10.5 and 12.5 ppm to acid sites in the 12-ring and 8-ring, respectively.[49] The higher chemical shift of 8-ring protons is related to their stronger acid strength, in agreement with the lower wavenumber for the O−H stretching vibration as observed with DRIFTS. An adequate fit of the two peaks is achieved for a number of spectra, suggesting 17% of the Brønsted acid sites are in the 8-ring for the MOR9-$Al_2(SO_4)_3$ sample. In contrast, the MOR6-$NaAlO_2$ sample has more protons in the constricted spaces of the 8-ring (23%). Commercial H-MOR has only 14% of protons in the 8-ring, continuing the trend now observed with TPD and DRIFTS.

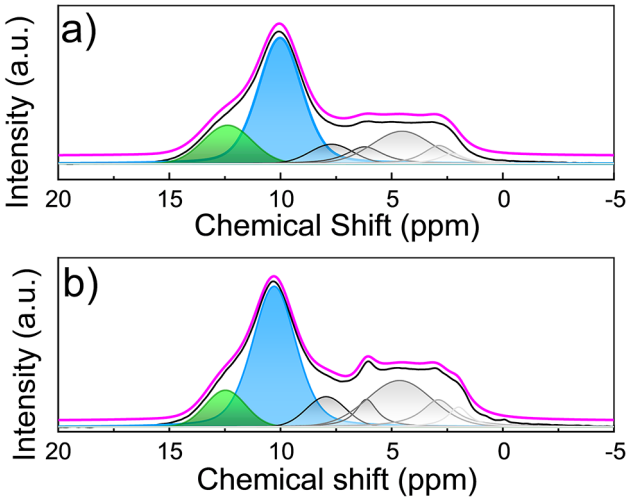

Figure 3. Adsorption of CD_3CN onto dehydrated MOR leading to the appearance of two new peaks at the expense of the 3.8 ppm peak.

2.2.4. CO Infrared Spectroscopy. Studying the samples by titrating acid sites at low temperatures (−196 °C) with CO (kinetic diameter 3.7 Å) further strengthened the evidence for having successfully altered the Al distribution in MOR. With increasing CO pressure, two peaks appear in the region between 2200 and 2080 cm^{-1} (Figure S9).[55] At 2170−2175 cm^{-1}, perturbed CO vibrations appear from the interaction with acid sites. At higher pressures, physisorbed CO gives rise to the band at 2138 cm^{-1}. It is apparent from the intensity of the perturbed CO vibrations that MOR6-$NaAlO_2$ has more acid sites, in line with the higher Al concentration. Furthermore, the peak shape is more symmetric. Lavalley et al. assign two species to the band centered at 2173 cm^{-1}, with CO adsorbed on acid sites in the 8-ring giving rise to a shoulder at 2169 cm^{-1} while those in the 12-ring appear at 2175 cm^{-1}.[55] These two species can be clearly distinguished at low to medium CO pressures in the MOR9-$Al_2(SO_4)_3$ sample. The more symmetric peak shape of the MOR6-$NaAlO_2$ sample results from a higher contribution of the species at 2169 cm^{-1}, in agreement with DRIFTS and ^{1}H MAS NMR. To assess and confirm the relative contribution of acid sites in the 12-ring and 8-ring, we attempted deconvolution of the IR band at 2173 cm^{-1} (Figure S10). In contrast to MOR6-$NaAlO_2$, a higher contribution of acid sites are located in the 12-ring for MOR9-$Al_2(SO_4)_3$, even at low CO pressures. While this result concurs with the trends observed with TPD, DRIFTS, and MAS NMR, dosing of CO does purport an overall higher relative concentration of acid sites in the 8-ring, irrespective of Al source (Figure 4).

2.2.5. Acid Site Accessibility. Figure 4 summarizes the four characterization techniques used to differentiate between acid sites in the 8- and 12-ring of MOR. There is an unmistakable trend toward higher acid site concentrations in the 12-ring when using $Al(NO_3)_3$ or $Al_2(SO_4)_3$ as the Al source. However, discrepancies for the individual techniques need to be rationalized. For the lab-synthesized, large MOR crystals, DRIFTS measures a higher concentration of acid sites in the 12-ring, compared to TPD results. The small crystals of the commercial H-MOR sample, however, agree well with TPD results, indicating a surface bias for the DRIFTS measurement.

https://doi.org/10.1021/acscatal.1c05091
ACS Catal. 2022, 12, 2166−2177

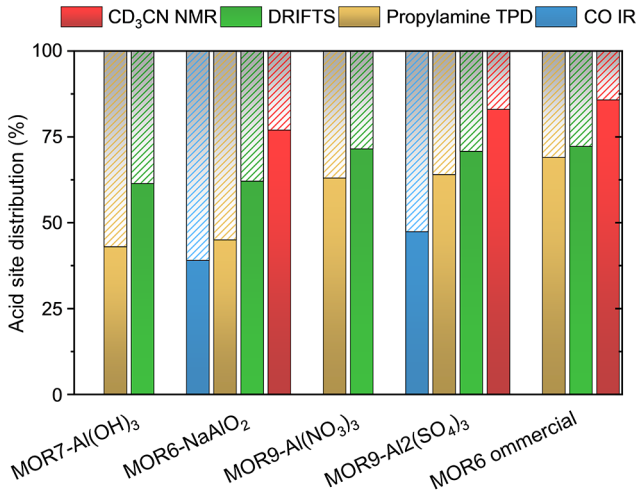

Figure 4. Acid site distributions for MOR zeolites discussed in this study as assessed with several different techniques. Color coding is used to illustrate the respective technique. The solid colored bars correspond to acid sites in the 12-ring (AI) with those in 8-rings making up the difference (patterned bars).

Even higher relative concentrations of acid sites in the 12-ring are obtained from dosing CD_3CN and probing with ^1H MAS NMR. Qualitatively, the spectra are comparable to those reported by Zheng et al.,[49,50] yet typical acid site distributions (12-ring vs 8-ring) in MOR are usually reported as 2:1 to 1:1.[44] This discrepancy could be associated with unknown molar extinction coefficients in IR spectra or a degree of sites in the 8-ring that cannot be titrated. The residual presence of the peak at 3.8 ppm post-adsorption would support the latter hypothesis. Finally, dosing of CO yields a good agreement with TPD results for the MOR6-$NaAlO_2$, while slightly diverging for MOR9-$Al_2(SO_4)_3$. We attribute this deviation to the inability of CO to differentiate between acid sites in the 8-ring and those situated in the 8-ring side pocket closer to the 12-ring, whereas n-propylamine can conceivably titrate these sites. Thus, we conclude that the miniscule pH changes in the synthesis gel, attributed to the dissociation of different Al precursors, impacts the Al distribution in MOR as evidenced by the subsequently probed acid site accessibility.

To prove this concept, we synthesized two additional MOR zeolites (Supporting Information). In the first case, we increased the Si/Al of MOR-$NaAlO_2$ from 6 to 8 to assess whether the accessibility index is an artifact of lower Si/Al ratios. The obtained zeolite, MOR8-$NaAlO_2$, showed comparable morphological and physicochemical properties to the previously synthesized MOR6-$NaAlO_2$. NH_4-TPD and NH_3-TPD were in line with the total Al and theoretical tetrahedral Al contents (Table 2). Most importantly, the accessibility index was 44% and thus comparable to those indices obtained for MOR6-$NaAlO_2$ and MOR7-$Al(OH)_3$.

The second proof-of-concept MOR synthesis aimed at confirming the impact of the pH. Synthesis of MOR with $Al_2(SO_4)_3$ was repeated; however, the gel was modified by the addition of more NaOH, increasing the ratio of OH^-/SiO_2 from 0.42 to 0.50. This increased the pH from 14.1 to 14.25. Consequently, the synthesized MOR had a slightly lower Si/Al of 8, a faster crystallization time (57 vs 88 h), and a smaller average particle diameter (17 vs 21 μm). Determining the accessibility index yielded a lower value (56%) compared to the parent MOR9-$Al_2(SO_4)_3$ (64%), which appears to confirm the successful modification of the Al site distribution on MOR as a function of the local pH.

In conclusion, it is evident how minor pH adjustments strongly affect the physicochemical properties of zeolites, with the inorganic cations and more importantly anions playing a structure-directing effect. Interestingly, the role of anions in zeolite synthesis has been investigated before by Kumar et al. showing that oxyanions, including SO_4^{2-}, can accelerate the formation process.[56,57] More recently, Yu et al. observed a similar crystallization rate enhancement by expanding the investigation to include the complete Hofmeister series (SO_4^{2-}, F^-, Cl^-, etc.).[58] They find that the OSDA molecule is surrounded not only by a hydration sphere, a clathrate model first proposed by Burkett and Davis,[59] but also by the anions that facilitate the release of water molecules from the hydration sphere and thus promote condensation of Si−O−Si bonds in the zeolite. Although this has been shown for high-silica zeolites, the synthesis of Al-rich FAU has also been shown to be influenced by the structuring of water molecules surrounding ions, in this case Na^+.[31,60] We do not observe any beneficial effect on the crystallization rate induced by the presence of oxyanions (SO_4^{2-} and NO_3^-) for MOR synthesis. It is strongly suggested that pH plays a dominant role in controlling the crystallization behavior. However, we do not want to exclude the very exciting possibility for these anions to influence the incorporation degree of Al into specific T-sites. Liu et al., for example, have highlighted the significance of gripper-like Si species to direct the spatial arrangement of heteroatoms,[61] a process that might very well be influenced by the presence of specific anions.

2.3. Towards the Direct Activation of CH_4.

Several authors have noted the significance of MOR with different acid site distributions, mainly with effect on the carbonylation of dimethylether, where acid sites in the 8-ring are exceptionally active.[45]

However, as pointed out above, the partial oxidation of CH_4 over MOR zeolites also exhibits a range of performances. Having successfully altered the acid site distributions in MOR, we now aim to investigate its impact on the productivity towards direct activation of CH_4 to MeOH over Cu-MOR. Copper is introduced via ionic exchange of aqueous copper acetate solutions at room temperature and a controlled pH of 5.2, the latter preventing the formation of copper nanoparticles.[62] In our previous study, different copper exchange degrees were achieved by changing the molarity of the Cu(acetate)$_2$ solution;[12] however, preliminary results suggested that the copper uptake in lab-synthesized H-MOR was severely limited compared to the commercial H-MOR (Figure S12a). The NH_4-MOR form, however, had a higher copper uptake. Higher exchange degrees were also attainable for the H-MOR forms at higher temperatures (60 °C) as well as when performing sequential exchange steps with intermediary drying steps. We were able to construct an exchange isotherm for the copper exchange at room temperature, as shown in Figure S12b.

From Figure S12b, it is evident that the large crystal size of the synthesized MOR hampers the transport of hydrated copper ions, $[Cu(H_2O)_6]^{2+}$. The long diffusion pathways in the crystal lattice prevent the hydrated copper ions from occupying all possible exchange sites. Instead, an intermediary drying step, removing the water ligands, allows the smaller Cu^{2+} ions to migrate to their final exchange location. This enables sequential exchanges to increase the copper loading in

https://doi.org/10.1021/acscatal.1c05091
ACS Catal. 2022, 12, 2166−2177

the zeolites. Intuitively, the more accessible the acid sites, the more readily a higher copper exchange degree is achieved, seen in Figure S12b.

Next, we assessed the performance of these Cu-MOR zeolites in the stepwise partial selective oxidation of CH_4. The reaction protocol follows our previously described methodology;[13] however, the CH_4 loading was shortened to 3 h without significantly affecting the total yield of the reaction.[63]

In our previous study, investigating copper exchanged on the commercial MOR highlighted that a Cu/Al ratio of <0.2 was optimal in terms of the MeOH productivity.[13] We therefore focused our study on two series of Cu-MOR across a range of copper loadings on the tetrahedral Al (i.e., $Cu/Al^{(IV)}$). No nanoparticles were observed in any of these samples as ascertained by backscattering electrons.[12] Unlike the materials reported by Lercher et al.,[11] our prepared Cu-MOR zeolites are not single-site catalysts as the amount of CH_4 activated per copper proceeds through a productivity maximum (Figure 5).

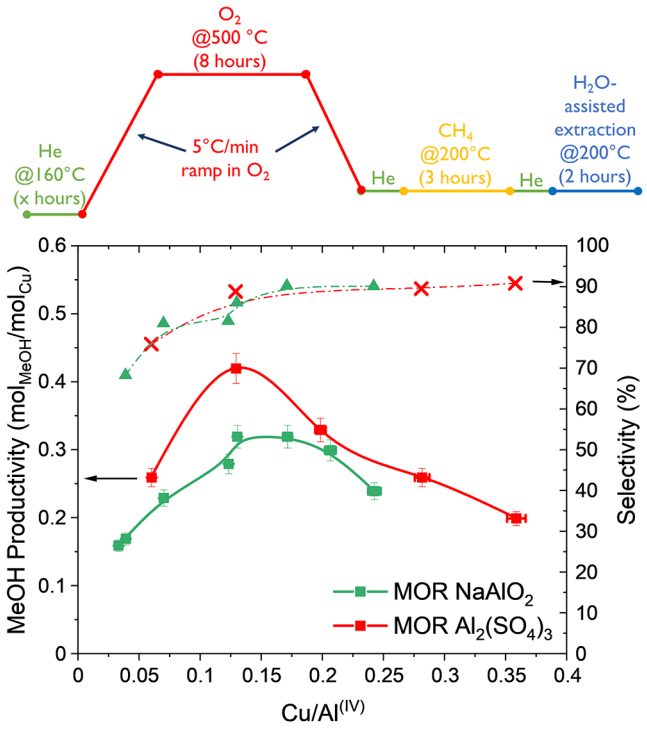

Figure 5. Partial oxidation of CH_4 as performed over MOR synthesized in-house using two different Al sources that generated high and low degrees of acid site accessibility. The reaction protocol is shown at the top. The data points are connected by a spline curve to illustrate the trend behavior.

At low exchange degrees, the MeOH selectivity is markedly lower at 70% and correlates with a lower productivity. The selectivity reaches and remains at a maximum of 90% in line with a maximum in productivity at intermediate exchange degrees. As the Cu loading is increased to nearly full exchange (i.e., Cu/Al 0.5), the efficiency of copper atoms to oxidize CH_4 to MeOH decreases. The volcano-type plots describe the formation of an optimum number of Cu-oxo sites as the copper loading is increased. At low exchange degrees, less selective copper sites are present, likely attributed to a lack of nearby copper atoms available for the formation of Cu-oxo dimers. Consequently, no selective oxidation to CO_2 occurs. As the loading is increased, more nearby sites are populated, enabling the formation of selective Cu-oxo species stabilizing methoxy intermediates and improving the overall MeOH productivity. Once the maximum number of active Cu-oxo sites is obtained, any additional copper behaves as a spectator, lowering the MeOH productivity at high loadings. These spectators appear to be inactive rather than nonselective, as evidenced by the continuously high MeOH selectivity. Note that this volcano-type behavior implies the significance of copper location in the framework. As demonstrated by the two investigated Cu-MOR series, their provenance also plays a crucial role in the maximum productivity obtained (Figure 5). MOR synthesized with $Al_2(SO_4)_3$ achieves a significantly higher maximum productivity (0.40 mol_{MeOH}/mol_{Cu}) than the MOR synthesized in the presence of $NaAlO_2$ (0.30 mol_{MeOH}/mol_{Cu}).

We have thus achieved, for the first time, the alteration of MeOH productivity over Cu-MOR by changing synthesis parameters, previously only shown for the SSZ-13 zeolite.[64] In that case, it was shown that Cu-oxo species situated near the double 6-ring and coordinated to two framework aluminum atoms are inactive. For MOR, however, no such synthesis−structure−activity relationship exists to date. Davis et al. observed that a Cu,Na-MOR system activates both less CH_4 and less selectively toward MeOH than a comparable Cu,H-MOR system.[17] They pointed out that Na^+ ions preferentially exchange on acid sites in the 8-ring, thus suggesting that the lower selectivity (70%) arises from the formation of Cu-peroxo sites, which require more space (e.g., in the 12-ring) than Cu-oxo dimers. It is clear that the two investigated Cu,H-MOR systems reported here have diverging activities while showing no differences in selectivity. Further, we can exclude Cu-Al-oxo extra-framework clusters as proposed by Lee et al. having an outsize role in explaining our reported material differences as we used both NH_4 and H forms for the ion exchange with copper.[52] It did not lead to distinct activity trends (Table S5). Instead, we postulate that the acid site accessibility degree induced by the Al site distribution influences the reactivity of the subsequently formed Cu-oxo species. MOR-$Al_2(SO_4)_3$ has conceivably fewer acid sites in the highly constricted 8-ring, and this correlates with a higher propensity for the activation of CH_4 than the MOR-$NaAlO_2$ counterpart across the whole Cu/Al range. The biggest improvement is achieved at intermediate exchange degrees. Here, the trend can also be extrapolated to the Cu-MOR previously reported by Pappas et al.[13] This sample is based on the commercial H-CBV10Ads, shown by the results above, to have a high degree of acid site accessibility (Table 2).

To underpin our hypothesis, we performed an ionic exchange with Co^{2+} ions to quantify the concentration of Al pairs. Acidic solutions of Co^{2+} ions preferentially exchange on paired Al sites.[20,65,66] The Langmuir-type cobalt-ion exchange isotherm of the acidic cobalt acetate solution (pH 3−4) showed comparable cobalt uptake for both MOR zeolites and the absence of cobalt oxide nanoparticles. This was irrespective of their Al source discounting varying degrees of Al pairing as a possible explanation for the differing MeOH productivity (Figure S13a).

2.4. Quantifying the Active Site with X-ray Absorption Spectroscopy (XAS). The active sites for the partial CH_4 oxidation in MOR have been suggested to be dimeric Cu-oxo species formed during the high-temperature activation procedure in oxygen.[13] Linear combination fitting of X-ray

https://doi.org/10.1021/acscatal.1c05091
ACS Catal. 2022, 12, 2166−2177

absorption near-edge spectroscopy (XANES) along with principal component analysis proposed that the most active Cu-oxo dimers are formed by self-reduction-resistant Cu^{2+} bound to the zeolite framework.[13] Utilizing XAS, we decided to look more closely at the synthesized Cu-MOR zeolites of different acid site accessibility. The XAS spectra of samples with medium and high Cu loading were obtained on sealed capillaries, pretreated in air at high temperatures. The XANES region of all spectra shows the features of a pure Cu^{2+} state, as previously described in detail.[13] The most productive sample, 0.11CuHMOR-$Al_2(SO_4)_3$, shows a differently shaped and higher white line (WL) than the rest of the samples. This, combined with a higher intensity in the first shell of the EXAFS region suggests that this sample has more uniform bond lengths and higher contributions from Cu−oxygen scatterings (Figure 6). From our previous studies, we can infer that this

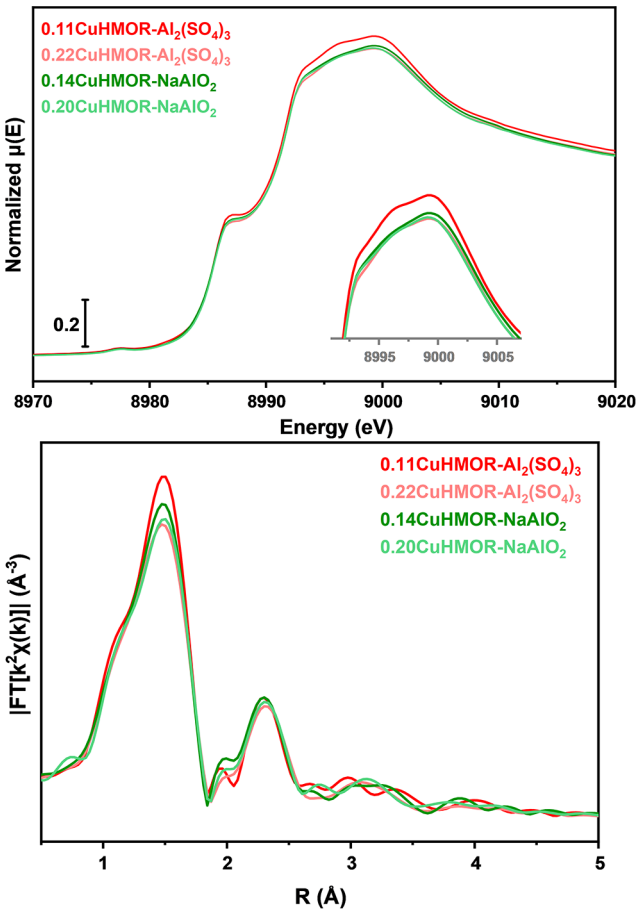

Figure 6. (Top) XANES spectra of the Cu K-edge for several activated Cu-MOR previously synthesized and tested for the partial oxidation of CH_4. (Bottom) EXAFS region highlighting the first shell interactions.

implies that the 0.11CuHMOR-$Al_2(SO_4)_3$ has a higher concentration of the highly active, self-reduction-resistant Cu^{2+} active sites compared to the $NaAlO_2$-based MOR. In addition, due to more Cu in less favorable positions in the higher Cu-loaded $Al_2(SO_4)_3$ MOR, we see that the XANES WL and EXAFS first shell are less intense also for this sample, compared to the medium loaded version of the same Al salt, likely a consequence of XAS being an averaging technique. Based on these spectroscopic results, the origin for the higher productivity of Cu-MOR-$Al_2(SO_4)_3$ lies in the larger concentration of active Cu-oxo dimers. This in turn implies the formation of self-reduction-resistant Cu^{2+} to be favored within the more accessible spaces of the MOR framework (i.e., not within the 8-ring channel). We can promote their concentration and the subsequent generation of more efficient Cu-oxo species by variations in zeolite formation, establishing a clear synthesis−structure−activity relationship.

3. CONCLUSIONS

We successfully altered the propensity of Cu-MOR for the partial oxidation of CH_4 by modifying intrinsic zeolite parameters, namely, the Al site distribution. This was accomplished by varying the choice of Al salt used in the synthesis gel leading to pH differences. Such small variations had a significant impact on the zeolite formation process. This leads to different aspect ratios of the micron-size crystals, altering the Al distribution in the framework and by extension the acid site and ion exchange site locations. A slightly lower pH promotes zeolite formation with acid sites situated in more accessible locations, away from the highly constricted 8-ring. This trend was captured via size discriminating base molecules, NH_3, and n-propylamine and further supported by observations made with DRIFTS, ^1H MAS NMR, and CO-IR. The correlation between inorganic Al source and intrinsic zeolite parameters was confirmed by variation of the gel pH, with a slightly higher pH leading to lower acid site accessibility, irrespective of the Si/Al ratio. The subsequently tested Cu-MOR systems showed diverging MeOH productivity as more accessible exchange sites promoted the formation of self-reduction-resistant Cu^{2+} sites, previously identified to lead to the most active pool of Cu-oxo dimers. The results reported herein indicate that the properties of the underlying zeolite support cannot be neglected and bear the potential for further improvement of the CH_4-to-MeOH conversion process.

4. EXPERIMENTAL PROCEDURE

4.1. Zeolite Synthesis. The synthesis was adapted from the IZA-verified synthesis reported by Kim and Ahn.[67] In a first step, 9.63 g of NaOH (99% VWR) was dissolved in 20 mL of H_2O. Then, 4.83 g of $NaAlO_2$ (50−56 wt % Al_2O_3, technical grade, Sigma-Aldrich) was added to the clear solution and stirred for 1 h. To the milky white solution, an additional 20 mL of H_2O was added and stirring was continued for an additional hour, during which the solution became clear. Then, 109 mL of H_2O was added, followed by the slow addition of 45 g of amorphous precipitated SiO_2 (Hi Sil 233, PPG Industries), gradually forming a dense gel. The gel composition was as follows: 5.9 Na_2O:Al_2O_3:28 SiO_2:318 H_2O. Alternative Al sources, used in equimolar Al_2O_3 amounts, were $Al(OH)_3 \times H_2O$ (50−57% Al_2O_3, Aldrich), $Al(NO_3)_3 \times 9H_2O$ (Sigma-Aldrich), and $Al_2(SO_4)_3 \times 18H_2O$ (98%, Sigma-Aldrich). This gel was aged at room temperature for 2 h with intermittent stirring before being placed in a Teflon-lined autoclave and allowed to crystallize at 170 °C under static conditions over the course of 24−96 h, depending on the gel composition and Al source. Upon completion, the autoclave was quenched and the solid powder isolated by filtration and washed with hot distilled water until a pH <10 was obtained. The samples were then dried at 70 °C overnight before undergoing further characterization. To obtain protonic zeolites, the as-synthesized Na-MOR was first exchanged 3× at 70 °C for 12 h with 1

https://doi.org/10.1021/acscatal.1c05091
ACS Catal. 2022, 12, 2166−2177

M NH_4NO_3 solution (20 mL/g). The NH_4-MOR was then calcined at 500 °C for 6 h (2 °C/min) in static air to decompose the ammonium cations.

4.1.1. Sample Nomenclature. *y*MOR*x*-"Al source" will be used as nomenclature to describe the various zeolites synthesized, with *x* representing the Si/Al ratio, *y* the Cu/Al ratio, and Al source being replaced by the respective Al salt.

4.1.2. Preparation of Cu Zeolites. Cu zeolites of varying Cu loading were obtained by exchanging either the NH_4 or H form of the synthesized MOR zeolites with aqueous 0.02 M $Cu(acetate)_2$ solution at room temperature for 4 h. Dropwise addition of NH_4OH increased the pH to 5.2. The pH was measured, using an electrode, at the beginning, after 2 h, and at the end to ensure that the pH was stable. As the exchange of Cu into the microporous system was limited at room temperature (see the Supporting Information, SI for exchange isotherm), samples with higher Cu loading were achieved by performing the exchange at 60 °C. After the exchange. the solids were separated from the solute via filtration, washed several times, and finally dried at 70 °C overnight. The samples were calcined at 500 °C before further characterization and/or testing. The samples were referenced based on their Cu/Al ratio rather than their specific exchange history.

4.2. Characterization. *4.2.1. X-ray Diffraction.* XRD patterns were collected on a Bruker D8 Discovery diffractometer using Cu Kα radiation (λ = 1.5418 Å). Experiments were run on a pressed powder sample holder in 2 theta range of 2−50° with a step size of 0.02°/s under ambient conditions.

4.2.2. N_2-Physisorption. N_2-physisorption isotherms were obtained using a BELSorp Maxi volumetric gas adsorption instrument (MicroTrac MRB) at −196 °C. Prior to analysis, the sample was evacuated at 300 °C for 10 h. The specific surface area was determined using the BET equation under pressure range relevant for microporous materials as defined by Rouquerol et al.[68] The total pore volume was obtained at p/p_0 0.99. The micropore volume was calculated based on the t-plot method.

4.2.3. Thermogravimetric Analysis (TGA). A Netzsch STA 449F Jupiter system was used to perform thermogravimetric analysis to determine the amount of physisorbed water on the zeolites. The material was heated to 1000 °C with a ramp rate of 5 °C/min under the flow of 50 mL/min synthetic air and 15 mL/min N_2.

4.2.4. Scanning Electron Microscopy (SEM). A Hitachi SU8230 microscope was used to obtain micrographs using a 1 kV acceleration voltage at a 10 μA current. Backscattering mode was used to identify any metallic clusters in Cu-exchanged zeolites.

4.2.5. Transmission Infrared Spectroscopy. IR spectra were measured on a Bruker Vertex 80 FT-IR spectrometer with an MCT detector. The material was pressed into a self-supporting wafer (15 mg) and placed inside a gold envelope within a homemade vacuum cell. The sample was activated in vacuum for 1.5 h at 450 °C before cooling to −196 °C with the help of liquid nitrogen. Then, about 20 mbar of CO was dosed onto the sample. After reaching equilibrium, the adsorbed CO was desorbed in a controlled manner, while simultaneously collecting spectra. The spectra were normalized to the overtones at 1871 cm^{-1}, and the spectrum collected before the introduction of CO was used as background for the background subtraction.

4.2.6. Diffuse Reflectance Infrared Fourier Transformed Spectroscopy (DRIFTS). DRIFTS spectra were obtained on a Bruker Vertex 70 FT-IR spectrometer using a Harrick Praying Mantis cell. Prior to measurement, a reference sample (KBr) was placed in the sample holder and a background was collected. Then, the reference sample was replaced by the material to be investigated and sample activation took place. The final spectra were collected at 380 °C after 1 h activation at 450 °C.

4.2.7. Temperature-Programmed Desorption (TPD). To probe the concentration of Brønsted acid sites, the acid-catalyzed Hoffman elimination of chemisorbed n-propylamine was studied in a homemade flow adsorption setup connected to a Pfeiffer Omnistar quadrupole mass spectrometer. First, ca. 50 mg of protonic zeolite was activated for 1 h at 500 °C (10 °C/min) in the flow of synthetic air (50 mL/min). After cooling the sample to 170 °C, the catalyst was exposed to saturated propylamine vapors in a N_2 carrier gas (50 mL/min) for 1 h. Physisorbed propylamine was then desorbed at the same temperature over the course of 4 h (66 mL/min N_2) followed by heating to 500 °C to generate propene. To quantify the amount of propene released, a calibrant gas was injected into the system at the end of the experiment. Additional experiments with varied N_2 flow rates verified that no released NH_3 readsorbed on the surface.

To quantify the total Al concentration, the NH_4 form was decomposed in a flow of N_2 (50 mL/min) heating to 600 °C at 10 °C/min, held for 1 h and cooled to 100 °C, and held for 5 h. The in situ generated acid sites were then titrated with NH_3 (2000 ppm in N_2) at 170 °C for 4 h. Once all sites were saturated, breakthrough of the NH_3 mass trace was observed and used to calibrate the NH_3 signal. Subsequently, physisorbed and weakly adsorbed NH_3 was removed from the sample by flushing with N_2 (66 mL/min) for 6 h. Finally, a second TPD step (66 mL/min N_2, 600 °C 10 °C/min) was performed to quantify the amount of NH_3 titrated on Brønsted acid sites.

4.2.8. Microwave Plasma Atomic Emission Spectroscopy (MP-AES). The elemental composition of the samples was determined with the help of an Agilent 4100 MP-AES instrument. Initially, the samples needed to be solubilized by dissolving ca. 20 mg of material in 1 mL of 15% hydrofluoric acid (HF) for 1 h in a Teflon liner. Complete dissolution was verified by the absence of solid particles when shining a light through the thin Teflon wall. Excess fluoride anions were bound by the addition of 5 wt % H_3BO_3, and the solution was diluted to 50 mL with distilled water. Quantification of the Si, Al, Na, and Cu contents was achieved using external calibration curves using commercial elemental standards.

4.2.9. Solid-State NMR. ^{27}Al MAS NMR measurements were performed on a Bruker Avance III spectrometer (11.74 T) located at SINTEF, Oslo (NO). Experiments were conducted in a 3.2 mm triple-resonance MAS probe at a spinning speed of 20 kHz. A single pulse sequence with a pulse length of 0.44 μs, corresponding to a 15° pulse angle and a recycle delay of 0.5 s, was used. A total of 10 000 scans were collected. The spectra were referenced to an aqueous $Al(NO_3)_3$ solution. The samples were hydrated over saturated $Ca(NO_3)_2$ solution for 48 h prior to the measurement.

^{1}H MAS NMR spectra were obtained using a 4 mm double-resonance probe at a spinning rate of 12 kHz with a single pulse sequence involving a 5 s recycle delay. A total of 800 scans were accumulated. The broad background in the proton spectra was subtracted using an empty rotor spectrum after bringing the spectra in-phase with each other. A 100 GHz

https://doi.org/10.1021/acscatal.1c05091
ACS Catal. 2022, 12, 2166−2177

Gaussian apodization and zero filling to 16k were used to enhance the spectra resolution. Prior to the measurement, the samples had to be dehydrated, which was achieved by connecting a glass tube to a vacuum manifold and pretreating the sample under vacuum at 450 °C for 16 h. The tube was then flame-sealed under vacuum and used to fill the rotor (with KF end-cap) in a glovebox. To titrate and identify specific acid sites, deuterated acetonitrile vapors were adsorbed onto the activated zeolite sample and allowed to equilibrate over the course of 2 h. Physisorbed CD_3CN was quickly removed, and the sample was flame-sealed under vacuum.

4.2.10. X-ray Absorption Spectroscopy. XAS experiments were performed at the BM31 beamline of the European Synchrotron Radiation Facility (ESRF) in Grenoble. Prior to the experiment, the samples were pretreated at 500 °C in air overnight before they were sealed and subsequently cooled down to room temperature. The thickness of the capillaries was chosen to be 1.5 mm, leading to a total absorption after the edge, μx, around 2.4. The edge jumps were in the 0.2−0.5 range. The Cu K-edge spectra of the samples were collected in transmission mode with the use of a water-cooled flat Si[111] double-crystal monochromator. He- and Ar-filled ionization chambers were used to measure the incident (I_0) and transmitted (I_1) X-ray intensities. The EXAFS scans were collected in the energy range of 8800−10 500 eV, with a constant energy step of 0.3 eV. The spectra were normalized to the unity edge jump using the Athena software from the Demeter package.[69] The $\chi(k)$ EXAFS functions were also extracted using the Athena software, and finally, by calculating the Fourier transform of the $k^2\chi(k)$ functions in the k range of 2.4−12.4 $Å^{-1}$, we obtained the Fourier transform (FT) EXAFS spectra.

4.3. CH_4 to MeOH Testing. Sieved Cu zeolites (100 mg, 250−425 mm) were placed in a glass tubular reactor containing a porous plug. The reactor was placed inside an oven and connected to the gas feed system and a Pfeiffer Quadstar Quadrupole Mass spectrometer. The sample was first dehydrated at 150 °C in He (15 mL/min) before changing to a flow of pure oxygen (100%, 15 mL/min) and activating the sample at 500 °C (5 °C/min) for 8 h. This time was chosen based on recent work on Cu-CHA to ensure that all Cu species are transformed to the active Cu-oxo sites.[64,70] Upon cooling to 200 °C, the sample was purged in He (15 mL/min) for 45 min and then exposed to a flow of CH_4 (100%, 15 mL/min) for 3 h. This was followed by another purging step (He, 15 mL/min, 30 min) and subsequently, methanol was extracted with a stream of 10% H_2O saturated Ne/He (15 mL/min) for 2 h. All of the gas lines after the water saturator were heated to ∼130 °C to prevent cold spots and condensation in the lines. The detected products were MeOH, dimethylether, and some carbon monoxide and carbon dioxide. The effluent was quantified using external conversion factors obtained from calibrant gases. Dry weights were used to normalize the amount of products formed.

■ ASSOCIATED CONTENT

Supporting Information

The Supporting Information is available free of charge at https://pubs.acs.org/doi/10.1021/acscatal.1c05091.

X-ray diffractograms, crystallization behavior of the synthesized zeolites, N_2-physisorption isotherms, TPD profiles, deconvoluted IR and ^1H MAS NMR spectra, ^{27}Al MAS NMR spectra, as well as physicochemical characterization of additionally synthesized materials,ion exchange isotherms and tabulated CH_4 activation data for reported materials (PDF)

■ AUTHOR INFORMATION

Corresponding Author

Sebastian Prodinger − *Center for Materials Science and Nanotechnology (SMN), Department of Chemistry, University of Oslo, 0315 Oslo, Norway;* orcid.org/0000-0001-8749-0476; Email: sebastian.prodinger@smn.uio.no

Authors

Karoline Kvande − *Center for Materials Science and Nanotechnology (SMN), Department of Chemistry, University of Oslo, 0315 Oslo, Norway*

Bjørnar Arstad − *SINTEF Industry, 0373 Oslo, Norway;* orcid.org/0000-0003-0398-786X

Elisa Borfecchia − *Department of Chemistry, NIS Center and INSTM Reference Center, University of Turin, 10125 Turin, Italy;* orcid.org/0000-0001-8374-8329

Pablo Beato − *Haldor Topsøe A/S, 2800 Kongens Lyngby, Denmark*

Stian Svelle − *Center for Materials Science and Nanotechnology (SMN), Department of Chemistry, University of Oslo, 0315 Oslo, Norway;* orcid.org/0000-0002-7468-5546

Complete contact information is available at: https://pubs.acs.org/10.1021/acscatal.1c05091

Notes

The authors declare no competing financial interest.

■ ACKNOWLEDGMENTS

The authors acknowledge the iCSI (industrial Catalysis Science and Innovation) Centre for Research based Innovation, which receives financial support from the Research Council of Norway under contract no. 237922. Furthermore, they would like to thank Elijah Aller for his exceptional glass-sculpting skills and Dr. Andrea Martini for performing XAS measurements. S.P. gratefully acknowledges Drs. Miroslaw Derewinski and Jingxiu Xie for lively scientific discussions and valuable input. Finally, PPG Industries is acknowledged for making the silica source samples available to the authors.

■ REFERENCES

(1) Saunois, M.; Stavert, A. R.; Poulter, B.; Bousquet, P.; Canadell, J. G.; Jackson, R. B.; Raymond, P. A.; Dlugokencky, E. J.; Houweling, S.; Patra, P. K.; Ciais, P.; Arora, V. K.; Bastviken, D.; Bergamaschi, P.; Blake, D. R.; Brailsford, G.; Bruhwiler, L.; Carlson, K. M.; Carrol, M.; Castaldi, S.; Chandra, N.; Crevoisier, C.; Crill, P. M.; Covey, K.; Curry, C. L.; Etiope, G.; Frankenberg, C.; Gedney, N.; Hegglin, M. I.; Höglund-Isaksson, L.; Hugelius, G.; Ishizawa, M.; Ito, A.; Janssens-Maenhout, G.; Jensen, K. M.; Joos, F.; Kleinen, T.; Krummel, P. B.; Langenfelds, R. L.; Laruelle, G. G.; Liu, L.; MacHida, T.; Maksyutov, S.; McDonald, K. C.; McNorton, J.; Miller, P. A.; Melton, J. R.; Morino, I.; Müller, J.; Murguia-Flores, F.; Naik, V.; Niwa, Y.; Noce, S.; O'Doherty, S.; Parker, R. J.; Peng, C.; Peng, S.; Peters, G. P.; Prigent, C.; Prinn, R.; Ramonet, M.; Regnier, P.; Riley, W. J.; Rosentreter, J. A.; Segers, A.; Simpson, I. J.; Shi, H.; Smith, S. J.; Paul Steele, L.; Thornton, B. F.; Tian, H.; Tohjima, Y.; Tubiello, F. N.; Tsuruta, A.; Viovy, N.; Voulgarakis, A.; Weber, T. S.; Van Weele, M.; Van Der Werf, G. R.; Weiss, R. F.; Worthy, D.; Wunch, D.; Yin, Y.; Yoshida, Y.; Zhang, W.; Zhang, Z.; Zhao, Y.; Zheng, B.; Zhu, Q.; Zhu,

Q.; Zhuang, Q. The Global Methane Budget 2000-2017. *Earth Syst. Sci. Data* **2020**, *12*, 1561−1623.
(2) Rorrer, J. E.; Beckham, G. T.; Román-Leshkov, Y. Conversion of Polyolefin Waste to Liquid Alkanes with Ru-Based Catalysts under Mild Conditions. *JACS Au* **2020**, *1*, 8−12.
(3) Gao, Y.; Jiang, J.; Meng, Y.; Yan, F.; Aihemaiti, A. A Review of Recent Developments in Hydrogen Production via Biogas Dry Reforming. *Energy Convers. Manage.* **2018**, *171*, 133−155.
(4) Gunsalus, N. J.; Koppaka, A.; Park, S. H.; Bischof, S. M.; Hashiguchi, B. G.; Periana, R. A. Homogeneous Functionalization of Methane. *Chem. Rev.* **2017**, *117*, 8521−8573.
(5) Groothaert, M. H.; Smeets, P. J.; Sels, B. F.; Jacobs, P. A.; Schoonheydt, R. A. Selective Oxidation of Methane by the Bis(μ-Oxo)Dicopper Core Stabilized on ZSM-5 and Mordenite Zeolites. *J. Am. Chem. Soc.* **2005**, *127*, 1394−1395.
(6) Newton, M. A.; Knorpp, A. J.; Sushkevich, V. L.; Palagin, D.; van Bokhoven, J. A. Active Sites and Mechanisms in the Direct Conversion of Methane to Methanol Using Cu in Zeolitic Hosts: A Critical Examination. *Chem. Soc. Rev.* **2020**, *49*, 1449−1486.
(7) Knorpp, A. J.; Newton, M. A.; Mizuno, S. C. M.; Zhu, J.; Mebrate, H.; Pinar, A. B.; Van Bokhoven, J. A. Comparative Performance of Cu-Zeolites in the Isothermal Conversion of Methane to Methanol. *Chem. Commun.* **2019**, *55*, 11794−11797.
(8) Narsimhan, K.; Iyoki, K.; Dinh, K.; Román-Leshkov, Y. Catalytic Oxidation of Methane into Methanol over Copper-Exchanged Zeolites with Oxygen at Low Temperature. *ACS Cent. Sci.* **2016**, *2*, 424−429.
(9) Dinh, K. T.; Sullivan, M. M.; Narsimhan, K.; Serna, P.; Meyer, R. J.; Dincă, M.; Román-Leshkov, Y. Continuous Partial Oxidation of Methane to Methanol Catalyzed by Diffusion-Paired Copper Dimers in Copper-Exchanged Zeolites. *J. Am. Chem. Soc.* **2019**, *141*, 11641−11650.
(10) IZA Structure Commission. http://www.iza-structure.org/ (accessed Aug 23, 2020).
(11) Grundner, S.; Markovits, M. A. C.; Li, G.; Tromp, M.; Pidko, E. A.; Hensen, E. J. M.; Jentys, A.; Sanchez-Sanchez, M.; Lercher, J. A. Single-Site Trinuclear Copper Oxygen Clusters in Mordenite for Selective Conversion of Methane to Methanol. *Nat. Commun.* **2015**, *6*, No. 7546.
(12) Dyballa, M.; Pappas, D. K.; Kvande, K.; Borfecchia, E.; Arstad, B.; Beato, P.; Olsbye, U.; Svelle, S. On How Copper Mordenite Properties Govern the Framework Stability and Activity in the Methane-to-Methanol Conversion. *ACS Catal.* **2019**, *9*, 365−375.
(13) Pappas, D. K.; Martini, A.; Dyballa, M.; Kvande, K.; Teketel, S.; Lomachenko, K. A.; Baran, R.; Glatzel, P.; Arstad, B.; Berlier, G.; Lamberti, C.; Bordiga, S.; Olsbye, U.; Svelle, S.; Beato, P.; Borfecchia, E. The Nuclearity of the Active Site for Methane to Methanol Conversion in Cu-Mordenite: A Quantitative Assessment. *J. Am. Chem. Soc.* **2018**, *140*, 15270−15278.
(14) Brezicki, G.; Kammert, J. D.; Gunnoe, T. B.; Paolucci, C.; Davis, R. J. Insights into the Speciation of Cu in the Cu-H-Mordenite Catalyst for the Oxidation of Methane to Methanol. *ACS Catal.* **2019**, *9*, 5308−5319.
(15) Snyder, B. E. R.; Vanelderen, P.; Schoonheydt, R. A.; Sels, B. F.; Solomon, E. I. Second-Sphere Effects on Methane Hydroxylation in Cu-Zeolites. *J. Am. Chem. Soc.* **2018**, *140*, 9236−9243.
(16) Zheng, J.; Lee, I.; Khramenkova, E.; Wang, M.; Peng, B.; Gutiérrez, O. Y.; Fulton, J. L.; Camaioni, D. M.; Khare, R.; Jentys, A.; Haller, G. L.; Pidko, E. A.; Sanchez-Sanchez, M.; Lercher, J. A. Importance of Methane Chemical Potential for Its Conversion to Methanol on Cu-Exchanged Mordenite. *Chem. - Eur. J.* **2020**, *26*, No. 7563.
(17) Brezicki, G.; Zheng, J.; Paolucci, C.; Schlögl, R.; Davis, R. J. Effect of the Co-Cation on Cu Speciation in Cu-Exchanged Mordenite and ZSM-5 Catalysts for the Oxidation of Methane to Methanol. *ACS Catal.* **2021**, *11*, 4973−4987.
(18) Dyballa, M.; Thorshaug, K.; Pappas, D. K.; Borfecchia, E.; Kvande, K.; Bordiga, S.; Berlier, G.; Lazzarini, A.; Olsbye, U.; Beato, P.; Svelle, S.; Arstad, B. Zeolite Surface Methoxy Groups as Key Intermediates in the Stepwise Conversion of Methane to Methanol. *ChemCatChem* **2019**, *11*, 5022−5026.
(19) Alberti, A. Location of Brønsted Sites in Mordenite. *Zeolites* **1997**, *19*, 411−415.
(20) Di Iorio, J. R.; Gounder, R. Controlling the Isolation and Pairing of Aluminum in Chabazite Zeolites Using Mixtures of Organic and Inorganic Structure-Directing Agents. *Chem. Mater.* **2016**, *28*, 2236−2247.
(21) Sobalik, Z.; Sazama, P.; Dedecek, J.; Wichterlová, B. Critical Evaluation of the Role of the Distribution of Al Atoms in the Framework for the Activity of Metallo-Zeolites in Redox N2O/NOx Reactions. *Appl. Catal., A* **2014**, *474*, 178−185.
(22) Pashkova, V.; Klein, P.; Dedecek, J.; Tokarová, V.; Wichterlová, B. Incorporation of Al at ZSM-5 Hydrothermal Synthesis. Tuning of Al Pairs in the Framework. *Microporous Mesoporous Mater.* **2015**, *202*, 138−146.
(23) Devos, J.; Robijns, S.; Van Goethem, C.; Khalil, I.; Dusselier, M. Interzeolite Conversion and the Role of Aluminum: Toward Generic Principles of Acid Site Genesis and Distributions in ZSM-5 and SSZ-13. *Chem. Mater.* **2021**, *3*, 2516−2531.
(24) Chen, L.; Falsig, H.; Janssens, T. V. W.; Jansson, J.; Skoglundh, M.; Grönbeck, H. Effect of Al-Distribution on Oxygen Activation over Cu-CHA. *Catal. Sci. Technol.* **2018**, *8*, 2131−2136.
(25) Di Iorio, J. R.; Li, S.; Jones, C. B.; Nimlos, C. T.; Wang, Y.; Kunkes, E.; Vattipalli, V.; Prasad, S.; Moini, A.; Schneider, W. F.; Gounder, R. Cooperative and Competitive Occlusion of Organic and Inorganic Structure-Directing Agents within Chabazite Zeolites Influences Their Aluminum Arrangement. *J. Am. Chem. Soc.* **2020**, *142*, 4807−4819.
(26) Biligetu, T.; Wang, Y.; Nishitoba, T.; Otomo, R.; Park, S.; Mochizuki, H.; Kondo, J. N.; Tatsumi, T.; Yokoi, T. Al Distribution and Catalytic Performance of ZSM-5 Zeolites Synthesized with Various Alcohols. *J. Catal.* **2017**, *353*, 1−10.
(27) Raatz, F.; Marcilly, C.; Freund, E. Comparison between Small Port and Large Port Mordenites. *Zeolites* **1985**, *5*, 329−333.
(28) Knorpp, A. J.; Pinar, A. B.; Newton, M. A.; Li, T.; Calbry-Muzyka, A.; van Bokhoven, J. A. Copper-Exchanged Large-Port and Small-Port Mordenite (MOR) for Methane-to-Methanol Conversion. *RSC Adv.* **2021**, *11*, 31058−31061.
(29) Lu, B.; Oumi, Y.; Sano, T. Convenient Synthesis of Large Mordenite Crystals. *J. Cryst. Growth* **2006**, *291*, 521−526.
(30) Prodinger, S.; Derewinski, M. A. Synthetic Zeolites and Their Characterization. In *Nanoporous Materials for Molecule Separation and Conversion*; Liu, J.; Ding, F., Eds.; Elsevier: Amsterdam, 2020; pp 65−88.
(31) Prodinger, S.; Vjunov, A.; Hu, J. Z.; Fulton, J. L.; Camaioni, D. M.; Derewinski, M. A.; Lercher, J. A. Elementary Steps of Faujasite Formation Followed by in Situ Spectroscopy. *Chem. Mater.* **2018**, *30*, 888−897.
(32) Zhang, L.; van Laak, A. N. C.; de Jongh, P. E.; de Jong, K. P. Synthesis of Large Mordenite Crystals with Different Aspect Ratios. *Microporous Mesoporous Mater.* **2009**, *126*, 115−124.
(33) Connick, R. E.; Fiat, D. N. Coordination Numbers of Beryllium and Aluminum Ions in Aqueous Solutions. *J. Chem. Phys.* **1963**, *39*, 1349−1351.
(34) Moolenaar, R. J.; Evans, J. C.; McKeever, L. D. Structure of the Aluminate Ion in Solutions at High PH. *J. Phys. Chem. A* **1970**, *74*, 3629−3636.
(35) Dai, W.; Kouvatas, C.; Tai, W.; Wu, G.; Guan, N.; Li, L.; Valtchev, V. Platelike MFI Crystals with Controlled Crystal Faces Aspect Ratio. *J. Am. Chem. Soc.* **2021**, *143*, 1993−2004.
(36) He, P.; Li, Y.; Cai, K.; Xiong, X.; Lv, J.; Wang, Y.; Huang, S.; Ma, X. Nano-Assembled Mordenite Zeolite with Tunable Morphology for Carbonylation of Dimethyl Ether. *ACS Appl. Nano Mater.* **2020**, *3*, 6460−6468.
(37) Li, Y.; Li, Z.; Huang, S.; Cai, K.; Qu, Z.; Zhang, J.; Wang, Y.; Ma, X. Morphology-Dependent Catalytic Performance of Mordenite in Carbonylation of Dimethyl Ether: Enhanced Activity with High c/b Ratio. *ACS Appl. Mater. Interfaces* **2019**, *11*, 24000−24005.

https://doi.org/10.1021/acscatal.1c05091
ACS Catal. 2022, 12, 2166−2177

(38) Bickel, E. E.; Nimlos, C. T.; Gounder, R. Developing Quantitative Synthesis-Structure-Function Relations for Framework Aluminum Arrangement Effects in Zeolite Acid Catalysis. *J. Catal.* **2021**, *399*, 75−85.
(39) Vjunov, A.; Fulton, J. L.; Huthwelker, T.; Pin, S.; Mei, D.; Schenter, G. K.; Govind, N.; Camaioni, D. M.; Hu, J. Z.; Lercher, J. A. Quantitatively Probing the Al Distribution in Zeolites. *J. Am. Chem. Soc.* **2014**, *136*, 8296−8306.
(40) Ravi, M.; Sushkevich, V. L.; van Bokhoven, J. A. Towards a Better Understanding of Lewis Acidic Aluminium in Zeolites. *Nat. Mater.* **2020**, *19*, 1047−1056.
(41) Di Iorio, J. R.; Bates, S. A.; Verma, A. A.; Delgass, W. N.; Ribeiro, F. H.; Miller, J. T.; Gounder, R. The Dynamic Nature of Brønsted Acid Sites in Cu-Zeolites During NOx Selective Catalytic Reduction: Quantification by Gas-Phase Ammonia Titration. *Top. Catal.* **2015**, *58*, 424−434.
(42) Corma, A. Inorganic Solid Acids and Their Use in Acid-Catalyzed Hydrocarbon Reactions. *Chem. Rev.* **1995**, *95*, 559−614.
(43) Kresnawahjuesa, O.; Gorte, R. J.; De Oliveira, D.; Lau, L. Y. A Simple, Inexpensive, and Reliable Method for Measuring Brønsted-Acid Site Densities in Solid Acids. *Catal. Lett.* **2002**, *82*, 155−160.
(44) Makarova, M. A.; Wilson, A. E.; Van Liemt, B. J.; Mesters, C. M. A. M.; De Winter, A. W.; Williams, C. Quantification of Brønsted Acidity in Mordenites. *J. Catal.* **1997**, *172*, 170−177.
(45) Bhan, A.; Allian, A. D.; Sunley, G. J.; Law, D. J.; Iglesia, E. Specificity of Sites within Eight-Membered Ring Zeolite Channels for Carbonylation of Methyls to Acetyls. *J. Am. Chem. Soc.* **2007**, *129*, 4919−4924.
(46) Lukyanov, D. B.; Vazhnova, T.; Cherkasov, N. B.; Casci, J. L.; Birtill, J. J.; Lukyanov, D. B.; Vazhnova, T.; Cherkasov, N.; Casci, J. L.; Birtill, J. J. Insights into Brønsted Acid Sites in the Zeolite Mordenite Insights into Brønsted Acid Sites in the Zeolite Mordenite. *J. Phys. Chem. C* **2014**, *118*, 23918−23929.
(47) Huo, H.; Peng, L.; Gan, Z.; Grey, C. P. Solid-State MAS NMR Studies of Brønsted Acid Sites in Zeolite H-Mordenite. *J. Am. Chem. Soc.* **2012**, *134*, 9708−9720.
(48) Müller, M.; Harvey, G.; Prins, R. Comparison of the Dealumination of Zeolites Beta, Mordenite, ZSM-5 and Ferrierite by Thermal Treatment, Leaching with Oxalic Acid and Treatment with SiCl4by1H,29Si And27A1 MAS NMR. *Microporous Mesoporous Mater.* **2000**, *34*, 135−147.
(49) Yi, X.; Xiao, Y.; Li, G.; Liu, Z.; Chen, W.; Liu, S. B.; Zheng, A. From One to Two: Acidic Proton Spatial Networks in Porous Zeolite Materials. *Chem. Mater.* **2020**, *32*, 1332−1342.
(50) Gong, K.; Liu, Z.; Liang, L.; Zhao, Z.; Guo, M.; Liu, X.; Han, X.; Bao, X.; Hou, G. Acidity and Local Confinement Effect in Mordenite Probed by Solid-State NMR Spectroscopy. *J. Phys. Chem. Lett.* **2021**, *12*, 2413−2422.
(51) Wang, M.; Jaegers, N. R.; Lee, M. S.; Wan, C.; Hu, J. Z.; Shi, H.; Mei, D.; Burton, S. D.; Camaioni, D. M.; Gutiérrez, O. Y.; Glezakou, V. A.; Rousseau, R.; Wang, Y.; Lercher, J. A. Genesis and Stability of Hydronium Ions in Zeolite Channels. *J. Am. Chem. Soc.* **2019**, *141*, 3444−3455.
(52) Lee, I.; Lee, M.-S.; Tao, L.; Ikuno, T.; Khare, R.; Jentys, A.; Huthwelker, T.; Borca, C. N.; Kalinko, A.; Gutiérrez, O. Y.; Govind, N.; Fulton, J. L.; Hu, J. Z.; Glezakou, V.-A.; Rousseau, R.; Sanchez-Sanchez, M.; Lercher, J. A. Activity of Cu−Al−Oxo Extra-Framework Clusters for Selective Methane Oxidation on Cu-Exchanged Zeolites. *JACS Au* **2021**, *1*, 1412−1421.
(53) Hu, J. Z.; Wan, C.; Vjunov, A.; Wang, M.; Zhao, Z.; Hu, M. Y.; Camaioni, D. M.; Lercher, J. A. ^{27} Al MAS NMR Studies of HBEA Zeolite at Low to High Magnetic Fields. *J. Phys. Chem. C* **2017**, *121*, 12849−12854.
(54) Prodinger, S.; Shi, H.; Wang, H.; Derewinski, M. A.; Lercher, J. A. Impact of Structural Defects and Hydronium Ion Concentration on the Stability of Zeolite BEA in Aqueous Phase. *Appl. Catal., B* **2018**, *237*, 996−1002.
(55) Maache, M.; Janin, A.; Lavalley, J. C.; Benazzi, E. FT Infrared Study of Brønsted Acidity of H-Mordenites: Heterogeneity and Effect of Dealumination. *Zeolites* **1995**, *15*, 507−516.
(56) Kumar, R.; Bhaumik, A.; Ahedi, R. K.; Ganapathy, S. Promoter-Induced Enhancement of the Crystallization Rate of Zeolites and Related Molecular Sieves. *Nature* **1996**, *381*, 298−300.
(57) Kumar, R.; Mukherjee, P.; Pandey, R. K.; Rajmohanan, P.; Bhaumik, A. Role of Oxyanions as Promoter for Enhancing Nucleation and Crystallization in the Synthesis of MFI-Type Microporous Materials. *Microporous Mesoporous Mater.* **1998**, *22*, 23−31.
(58) Sun, C.; Liu, Z.; Wang, S.; Pang, H.; Bai, R.; Wang, Q.; Chen, W.; Zheng, A.; Yan, W.; Yu, J. Anionic Tuning of Zeolite Crystallization. *CCS Chem.* **2021**, *3*, 189−198.
(59) Burkett, S. L.; Davis, M. E. Mechanism of Structure Direction in the Synthesis of Pure-Silica Zeolites. 2. Hydrophobic Hydration and Structural Specificity. *Chem. Mater.* **1995**, *7*, 1453−1463.
(60) Flanigen, E. M. A Review and New Perspectives in Zeolite Crystallization. *Adv. Chem.* **1973**, *121*, 119−139.
(61) Chen, Z.; Liu, X.; Yu, Y.; Tang, Z.; Wang, J.; Liu, D.; Fang, N.; Lin, Y.; Liu, Y.; He, M. Gripper-like Silicon Species for Efficient Synthesis of Crystalline Metallosilicates with Spatially Homogeneous Heteroatoms in the Framework. *Chem. Mater.* **2021**, *33*, 4988−5001.
(62) Grundner, S.; Luo, W.; Sanchez-Sanchez, M.; Lercher, J. A. Synthesis of Single-Site Copper Catalysts for Methane Partial Oxidation. *Chem. Commun.* **2016**, *52*, 2553−2556.
(63) Kvande, K.; Pappas, D. K.; Dyballa, M.; Buono, C.; Signorile, M.; Borfecchia, E.; Lomachenko, K. A.; Arstad, B.; Bordiga, S.; Berlier, G.; Olsbye, U.; Beato, P.; Svelle, S. Comparing the Nature of Active Sites in Cu-Loaded SAPO-34 and SSZ-13 for the Direct Conversion of Methane to Methanol. *Catalysts* **2020**, *10*, No. 191.
(64) Pappas, D. K.; Borfecchia, E.; Dyballa, M.; Pankin, I. A.; Lomachenko, K. A.; Martini, A.; Signorile, M.; Teketel, S.; Arstad, B.; Berlier, G.; Lamberti, C.; Bordiga, S.; Olsbye, U.; Lillerud, K. P.; Svelle, S.; Beato, P. Methane to Methanol: Structure-Activity Relationships for Cu-CHA. *J. Am. Chem. Soc.* **2017**, *139*, 14961−14975.
(65) Khivantsev, K.; Derewinski, M. A.; Jaegers, N. R.; Boglaienko, D.; Hernandez, X. I. P.; Pearce, C.; Wang, Y.; Szanyi, J. *Increasing Al-Pair Abundance in SSZ-13 Zeolite via Zeolite Synthesis in the Presence of Alkaline Earth Metal Hydroxide Produces Hydro-Thermally Stable Cobalt and Pd-SSZ-13 Materials for Pollutant Abatement Applications*; ChemRxiv, 2021.
(66) Dědeček, J.; Kaucký, D.; Wichterlová, B.; Gonsiorová, O. Co 2+ Ions as Probes of Al Distribution in the Framework of Zeolites. ZSM-5 Study. *Phys. Chem. Chem. Phys.* **2002**, *4*, 5406−5413.
(67) Kim, G. J.; Ahn, W. S. Direct Synthesis and Characterization of High-SiO2-Content Mordenites. *Zeolites* **1991**, *11*, 745−750.
(68) Llewellyn, P.; Reinoso, F. R.; Rouquerol, J.; Seaton, N. Characterization of Porous Solids VII. In *Studies in Surface Science and Catalysis*; Elsevier, 2006; Vol. *160*, p 748.
(69) Ravel, B.; Newville, M. ATHENA, ARTEMIS, HEPHAESTUS: Data Analysis for X-Ray Absorption Spectroscopy Using IFEFFIT. *J. Synchrotron Radiat.* **2005**, *12*, 537−541.
(70) Bregante, D. T.; Wilcox, L. N.; Liu, C.; Paolucci, C.; Gounder, R.; Flaherty, D. W. Dioxygen Activation Kinetics over Distinct Cu Site Types in Cu-Chabazite Zeolites. *ACS Catal.* **2021**, *11*, 11873−11884.

https://doi.org/10.1021/acscatal.1c05091
ACS Catal. 2022, 12, 2166−2177